McBeck, J., Mair, K., Renard, F. (2018) Linking macroscopic failure with micromechanical processes in layered rocks: How layer orientation and roughness control macroscopic behavior. Tectonophysics, https://doi.org/10.1016/j.tecto.2018.11.016.

Linking macroscopic failure with micromechanical processes in layered rocks: How layer orientation and roughness control macroscopic behavior

Jessica McBeck[1], Karen Mair[1,2], François Renard[1,3]

1 Physics of Geological Processes, The Njord Centre, Department of Geosciences, University of Oslo, Norway
2 currently on sabbatical at: School of Geosciences, University of Edinburgh, Scotland
3 University Grenoble Alpes, University Savoie Mont Blanc, CNRS, IRD, IFSTTAR, ISTerre, 38000 Grenoble, France

Corresponding author
Jessica McBeck
j.a.mcbeck@geo.uio.no

Abstract

To constrain the impact of preexisting mechanical weaknesses on strain localization culminating in macroscopic shear failure, we simulate triaxial compression of layered sedimentary rock using three-dimensional discrete element method simulations. We develop a novel particle packing technique that builds layered rocks with preexisting weaknesses of varying orientations, roughness, and surface area available for slip. We quantify how the geomechanical behavior, characterized by internal friction coefficient, μ_0, and failure strength, σ_F, vary as a function of layer orientation, θ, interface roughness, and total interface area. Failure of the simulated sedimentary rocks mirrors key observations from laboratory experiments on layered sedimentary rock, including minima σ_F and μ_0 for layers oriented at 30° with respect to the maximum compressive stress, σ_1, and maxima σ_F and μ_0 for layers oriented near 0° and 90° to σ_1. The largest changes in σ_F (66%) and μ_0 (20%) occur in models with the smoothest interfaces and largest interface area. Within the parameter space tested, layer orientation exerts the most significant impact on σ_F and μ_0. These simulations allow directly linking micromechanical processes observed within the models to macroscopic failure behavior. The spatial distributions of nucleating microfractures, and the rate and degree of strain localization onto preexisting weaknesses, rather than the host rock, are systematically linked to the distribution of failure strengths. Preexisting weakness orientation more strongly controls the degree and rate of strain localization than the imposed confining stress within the explored parameter space. Using the upper and lower limits of μ_0 and σ_F obtained from the models, estimates of the Coulomb shear stress required for failure of intact rock within the upper seismogenic zone (7 km) indicates that a rotation of 30° of σ_1 relative to the weakness orientation may reduce the shear stress required for failure by up to 100 MPa.

Keywords: Anisotropy; preexisting weakness; layered rock; internal friction; failure strength; discrete element method

1. Introduction

Natural rocks contain mechanical weaknesses that span several orders of magnitude in scale, from grain contacts to plate boundary faults. In particular, sedimentary basins host layers of sediments and sedimentary rocks at various stages of deposition, burial, diagenesis and lithification that may provide mechanical weaknesses along their contacts. Bedding-parallel fractures between strata (e.g., Gale et al., 2014), and bedding-perpendicular fractures that terminate at layer contacts (e.g., Pollard & Aydin, 1988) demonstrate that interfaces between sedimentary strata can act as mechanical weaknesses that influence stresses, localize strain and impact macroscopic failure.

However, many numerical models of crack growth and fault development assume homogeneous and isotropic host rock properties due, in part, to the scarcity of field and laboratory data that constrain precisely how preexisting weaknesses impact the macroscopic geomechanical behavior of the host rock. To constrain the influence of preexisting mechanical weaknesses on macroscopic failure, we execute series of triaxial compression tests on discrete element method simulations of layered sedimentary rock. We designed a new DEM layer construction technique in order to capture mechanical anisotropy that arises from differences in lithology and unconformities in layered sequences. We vary the layer orientation with respect to the maximum compression direction, the layer interface roughness, the total layer interface area available for slip, and the applied confining stress. We assess the impact of each parameter on the concentration of microscopic failure along the preexisting weaknesses relative to diffuse deformation throughout the host rock, and on the resulting macroscopic failure stress and internal friction. Although previous experiments have investigated the impact of layer orientation on failure strength (e.g., Duveau et al., 1998), this numerical analysis is the first to compare the relative impact of each of the aforementioned parameters on failure behavior, and the first to investigate differences produced by layer interface roughness and area. The new layer construction technique is critical to this parameterization. Furthermore, we directly link the spatial distribution of microfracturing and strain localization to macroscopic geomechanical response, thus providing new insights not yet available experimentally.

2. Influence of mechanical weaknesses on failure

Due to the prevalence of materials containing mechanical weaknesses, many experimentalists have worked to understand how mechanical weaknesses impact rock failure and elastic properties (e.g., Duveau et al., 1998). Many experiments have focused on the peak failure strength of materials (e.g., Donath, 1961, 1964; Nova and Zaninetti, 1990; Shea and Kronenberg, 1993; Duveau et al., 1998; Cho et al., 2012; Fjær and Nes, 2014). For example, increasing mica content in foliated gneiss decreases the compressional strength because biotite grains provide nucleation sites for tensile microcracks (Rawling et al., 2002). Similarly, compression tests on Mancos shale indicate that bedding planes are weak relative to the host rock and tend to fail preceding macroscopic failure (Fjær and Nes, 2014). Here, we aim to capture differences in mechanical behavior that arise in layered sedimentary rock.

Internal friction is an empirical term that experimentalists identify from the slope of linear regression fits through experimental measurements of the stress conditions at or immediately preceding failure (e.g., Byerlee, 1978). The internal friction and peak failure stress provide estimates of the stress state at which rocks fail, and so are critical in robust predictions of brittle failure within intact material at varying crustal conditions. Although many experiments have identified relationships between the orientation of preexisting mechanical weaknesses and failure stress (e.g., Shea and Kronenberg, 1993; Tavallali and Vervoort, 2010), few have attempted to constrain the impact of planar mechanical weaknesses on the internal friction of the host rock (e.g., Donath, 1961; Duveau et al., 1998). This gap in understanding arises from the necessity of breaking multiple rock cores at varying confining stresses in order to identify a relationship between an applied confining stress and resulting failure stress, and so estimate internal friction. Consequently, to robustly constrain internal friction and hence predict the conditions of brittle rock failure at depth, experimentalists must use rock samples that are sufficiently similar to each other so that the suite of experiments at varying confining stresses mimic the same characteristic rock core. In addition, to characterize how microstructures are evolving and localizing with accumulated strain requires labor-intensive serial experimentation in which tests on similar rock cores are stopped at systematic strain increments (e.g., Mair et al., 2000). These tasks become increasingly challenging when focusing on rocks with well-developed mechanical anisotropy.

In contrast to laboratory experiments, numerical simulations allow the deformation of identical simulated rock containing mechanical weaknesses under a range of loading conditions. Consequently, the natural variability between individual rock cores that often plague experimental work does not have a strong influence on resulting geomechanical behavior in numerical models. Furthermore, numerical methods enable systematic comparison of mechanical properties of material with differing expressions of heterogeneity (e.g., Hentz et al., 2004; Belheine et al., 2009; Scholtès & Donzé, 2012, 2013; Dinç & Scholtès, 2018), such as layers with differing orientations and roughness, as in this study. Numerical models provide new insights into how evolving microstructures control macroscopic behavior (e.g., Schöpfer et al., 2009) that are generally not available in situ from laboratory experiments, unless the experimentalists use techniques such as recording acoustic emissions (e.g., Stanchits et al., 2006) or acquiring tomograms (e.g., Renard et al., 2018), from which they infer the evolving fracture network. Post-deformation procedures required after laboratory triaxial experiments, such as unloading and epoxy impregnation for microscopic analyses, may alter or overprint the microstructures. These procedures are not necessary for assessing microstructural evolution within numerical models, and so deciphering such microstructural artifacts is not necessary.

3. Methods

To constrain the impact of preexisting mechanical weaknesses on macroscopic geomechanical properties, we simulate triaxial compression of layered sedimentary rock using the discrete element method modeling tool ESyS-Particle. We briefly introduce the underlying physics of this tool. Then we describe the details of the models used in this study, including the model loading conditions, model microparameters, calibration, and a novel particle packing technique to construct the sedimentary layers.

3.1. ESyS-Particle

We triaxially compress simulated layered sedimentary rock using the parallel 3D discrete element method (DEM) simulation package ESyS-Particle (Abe et al., 2003). Similar to other DEM approaches (e.g., Cundall and Strack, 1979), ESyS-Particle simulates rock with many individual spherical particles that are initially connected by elastic bonds that may fail following a tensile criterion or the Coulomb shear failure criterion. The underlying physics implemented in ESyS-Particle and other DEM implementations, such as YADE, are similar, although details of the packing algorithms, contact laws and failure criteria differ.

ESyS-Particle simulations of fault gouge production produce realistic evolutions of fault gouge size and sliding friction (Abe and Mair, 2005, 2009; Mair and Abe, 2008). The 3D implementation of ESyS-Particle enables out-of-plane motion, which has proven important to fault gouge production (Hazzard and Mair, 2003; Abe and Mair, 2005; Mair and Hazzard, 2007).

These DEM simulations provide additional information beyond that available from laboratory experiments, such as directed force networks, at fine spatiotemporal resolution throughout deformation (e.g., Mair and Hazzard, 2007).

3.2. Construction of layered rock

To simulate triaxial compression tests of layered sedimentary rock using ESyS-Particle, we build particle assemblages containing layers that are separated by preexisting weaknesses, representing layered sedimentary rock. We build sample geometries of blocks (cuboids) with length to width ratio 2:1 and cubes (ratio 1:1). We investigate both cubes and blocks because the model shape influences the total layer interface area available for slip, and in particular, how many bonds connect particles within layers (i.e., host rock matrix) and between layers (i.e., interfaces) for each layer orientation. Comparing the results from these sets of models highlights the influence of the total layer interface area available for slip on rock failure. The dimensions of the cubes are 20 mm, while the dimensions of the rectangular blocks are 20 mm, 20 mm and 40 mm, with the long axis oriented vertically, parallel to σ_1 (Fig. 1). The model dimensions constrain the choice of layer thickness (5 mm). This thickness allows the macroscopic failure behavior to be independent of the specific particle packing geometry of one or two layer interfaces because models include at least 4 layers. Here, we do not assess the influence of layer thickness on failure behavior because this influence likely scales with the model volume, and so may not yield significant insights into crustal deformation. In particular, the failure of a larger model with thicker layers may be similar to the failure of a smaller model with thinner layers if the total interface area available for slip are similar. In order to assess the influence of total interface area of failure behavior, we change the shape of the model rather than the thickness of the layers.

To assess the influence of preexisting weaknesses on internal friction, we vary the orientation of layers, and keep the direction of maximum compression constant (vertical). We measure layer orientation, θ, as the clockwise angle from the top side of the model to the layer interface (Fig. 1), which is also the angle between σ_1 and the normal to the layer interface. Horizontal layers have θ=0°, and vertical layers have θ=90°. The layers are parallel in the z-dimension, which is the out of plane direction.

We develop a novel particle packing technique in order to build layers of varying interface roughness. We construct polygonal volumes and then fill the volumes with spherical particles with radii of 0.1 mm to 1.0 mm (Fig. S1). We fill the volumes with particles starting from the bottom volume and working upward, or in the case of vertical layers, from left to right. We fill each volume using a standard particle packing technique of ESyS-Particle that has produced DEM models that match the macroscopic behavior of brittle elastic materials. Then we connect neighboring particles inside each layer with bonds, as well as the particles between each layer. The variability in particle packing, and hence porosity, across layer interfaces are small. In order to capture differences in mechanical strength along layer interfaces, we set the cohesion of bonds within layers (i.e., host rock) to 20 MPa and set the cohesion of bonds between layers (i.e., preexisting weaknesses) to 10 MPa. Calibration of the numerical failure strengths to experimental strengths constrain the cohesion of bonds within the layers. The precise ratio of the strength of the host rock and interfaces remains one of the least constrained by experimental data. In addition, the effective strength of the interfaces arises from both the chosen cohesion and particle packing across layer interfaces, as discussed below.

In ESyS-Particle, the bond tensile strength is determined from the microparameter Mohr-Coulomb criterion constructed from the bond internal friction and cohesion. Extension of the criterion into the tensile normal stress regime determines the bond tensile strength. ESyS-Particle allows the application of a truncation factor to reduce the tensile strength from that predicted by the Mohr-Coulomb criterion, but we did not employ this factor here. Consequently, the advantage of parameterizing the cohesion rather than a different microparameter is that doing so changes both the tensile and shear failure criterions. The microparameters of bonds within each layer are identical. The bonds within layers are stronger than the bonds between layers, and are subsequently referred to as strong and weak bonds, respectively. The lack of employed truncation factor may produce larger tensile macroscopic strengths than natural sedimentary rocks, and so amplify the influence of shear failure relative to tensile failure.

To control the initial roughness of the layer interfaces (Fig. 2), we change the potential spatial overlap of the adjacent layers (Fig. S1). This overlap parameter specifies how many millimeters by which the boundaries of neighboring polygonal volumes overlap. With an overlap of 1 mm, for example, the vertical position of the bottom of a horizontal layer is 1 mm lower than the vertical position of the top of the previous (lower) horizontal layer (Fig. S1). With increasing overlap, particles are more closely packed along layer interfaces, and produce greater roughness (Fig. S1, Fig. 2). The bottom surface of each layer interface is smoother than the top surface because we pack the models starting from the bottom of the model (Fig. S1, Fig. 2).

A key question is whether the effective strengths of the simulated layer interfaces are comparable to the strengths of layer interfaces in natural sedimentary strata, or other mechanical weaknesses found in the crust. Both the bond cohesion and packing geometry along layer interfaces influence the effective strength of the layer interface. However, the packing geometry appears to exert a stronger influence than the bond cohesion. With zero grain overlap and no applied confining stress, some models fail immediately after the particles experience gravitational forces because the particles do not geometrically interlock across the layer interfaces. This lack of interlocking produces exceptionally smooth surfaces that provide little resistance to gravity.

The slip-parallel and slip-perpendicular root-mean-squared roughness, χ_{RMS}, of slip surfaces acquired from white light interferometer measurements (Renard et al., 2012) constrain the potential range of χ_{RMS} of intact sedimentary interfaces (Fig. S2). Although the χ_{rms} of intact interfaces are likely higher than the χ_{RMS} of slipped surfaces, we expect that the slip-perpendicular and slip-parallel roughness are on the same order of magnitude of the intact interfaces. For example, in clay-rich sandstone and shales with a mean grain size, *G*, the finest roughness is expected on to be on the scale of approximately 0.5*G*. However, there may be random pitting on the order of a few millimeters due to local differential compaction or displacements of grains during sedimentation. In the numerical models, we measure χ_{RMS} by identifying the layers of particles that connect adjacent layers, rotating the exposed layer contacts so that they trend horizontal, and finding the elevation of each particle from the particle radius and the y-coordinate (vertical) of the particle centroid. The resulting surface of particle elevations reflects the roughness of the layer contact. The overlap distances of 0.2 mm and 0.5 mm produce layer interfaces with χ_{RMS} that overlap the ranges of the laboratory measurements of slip-perpendicular and slip-parallel χ_{RMS} (Fig. S2).

With this particle packing technique, the particle radii range (0.1-1.0 mm) limits the maximum χ_{RMS} achievable in the models, similar to the grain size in sedimentary rock. When the overlap is greater than 0.5 mm, the χ_{RMS} remains relatively constant because increasing the overlap does not allow denser particle packing between layers with the selected particle radii range. Despite these constraints, the χ_{RMS} produced along the numerical layer interfaces compares favorably with physical measurements of χ_{RMS}, lending confidence to the ability of the models to capture the onset of macroscopic failure in layered sedimentary rock. These estimates of roughness with χ_{RMS} may be used to estimate the corresponding joint roughness coefficient (JRC) using empirical statistical relationships between JRC and χ_{RMS} (e.g., Tse & Cruden, 1979).

This particle packing technique produces models with porosities that differ by <1-2%. The porosity of models with layers with both overlap values range from 24-25%, and models with no layers have 23% porosity. Consequently, the variability in porosities between models is analogous to natural variability.

Previous numerical studies have assessed anisotropy with DEM models using numerical objects that behave as joints (e.g., Scholtès and Donzé, 2012). One central difference between our implementation of anisotropy and these methods is that our approach enables modifying the roughness of preexisting weaknesses. Consequently, our approach is more applicable to sedimentary rocks constructed from the sediment deposition in which sediments and clays gravitationally settle on top of older sediments, rather than jointed rock masses, for example.

3.3. Calibration

To simulate laboratory triaxial compression tests, we first apply linearly increasing confining stress, from zero to the desired stress, on each of the six sides of the model such that $\sigma_1=\sigma_2=\sigma_3$. Next, we displace the top and bottom sides synchronously at a constant velocity (0.125 mm/s) toward the center of the model, increasing σ_1 while maintaining $\sigma_2=\sigma_3$. Once the maximum desired loading velocity is reached, we continue to apply this velocity for several thousand time steps until after the sample fails.

The low applied velocity, linear ramp of the confining stress and loading velocity, and the symmetrically loading of the top and bottom edges, enhances stability of the particle assemblage by ensuring quasi-static conditions. In addition to these precautions, we calculate an appropriate model time step length following the Courant condition (Courant et al., 1928), where the numerically stable time step, d_t, is related the minimum particle mass, M_{min}, and maximum bond stiffness, K_{max}, as

$$d_t < 0.1 \sqrt{\frac{M_{min}}{K_{max}}} \qquad \text{Eq. 1}$$

Systematic tests conducted with varying bond and particle parameters (Table S1) produce uniaxial compressive strengths (40-120 MPa) within the range of natural layered shale (e.g., Cho et al., 2012).

Table S1 shows the values of microparameters that were constrained by careful calibration. Pairs of bonded and unbonded particles have frictional and elastic interactions. We calculate the corresponding particle density using the initial porosity of the model, ϕ (25%), and a desired bulk density of 2700 kg/m^3, ρ, such that the particle density is ρ(1-ϕ). We then follow the established numerical technique of increasing the particle density by a factor of 10^6, which enables larger time step lengths and thus shorter run times. Following the Courant condition (Eq. 1), the minimum particle radius and maximum bond stiffness determine the time step length. The ramp up times are sufficiently long to produce stable models in which the total kinetic energy does not increase unbounded. Particles interact with the walls that apply the constant velocity or force boundary conditions with elastic interactions following the prescribed stiffness, and without frictional interactions. The tensile strength of the bonds is determined by extrapolation of the Mohr-Coulomb failure criterion using the bond microparameters of internal friction and cohesion. The microparameters of the bonded and unbonded particles are not expected to equal physical values of those properties. Instead, we calibrate the microparameters to produce bulk macroscopic properties of the models that are within the range of physical measurements.

The failure of these simulated sedimentary rocks mirrors key observations from laboratory experiments, including: failure envelopes that decrease in slope at higher confining stresses, σ_2, broadening loading curves near peak stresses at higher σ_2, and smaller stress drops at higher σ_2. Similarly consistent with laboratory experiments, σ_F and μ_0 are minimized for layers oriented at 30° with respect to σ_1, and maximized for layers oriented near 0° and 90° to σ_1. These observations provide further evidence of robust calibration, and applicability of the numerical results to crustal behavior. These observations are discussed in greater detail in the next section.

Furthermore, these loading conditions, microparameters and particle packing technique produce models with bulk geomechanical responses that are not sensitive to location of individual particles (Fig. S3). In particular, the stress-strain curves of models that differ only in the location of initial seed points, which determine the random packing of particles, match along >90% of their length preceding macroscopic failure, have comparable means and magnitudes of fluctuations after failure, and produce similar failure stresses (Fig. S3).

The numerical models employed here benefit from several years of software development and benchmark calibration (e.g., Weatherley et al., 2010; Schopfer et al., 2009; Mair and Abe, 2009). Consequently, we selected several model parameters, such as the ratio of the minimum to maximum particle radii (0.1/1.0), using results from previous calibrations that produce model behaviors that closely match the behavior of linear elastic brittle materials.

3.4. Internal friction derivation

To constrain the macroscopic internal friction, μ_0, of each simulated layered sedimentary rock, we execute triaxial compression tests at increasing confining stress, $\sigma_2 = \sigma_3$. We test σ_2

from 0-50 MPa in models with differing layer orientations (from horizontal to vertical layers), differing layer interface roughness (0.2 mm or 0.5 mm overlap) and differing total layer interface area (cube or block models), requiring more than 256 unique model runs (Table S.2). In order to compare the geomechanical responses of layered rock to more homogeneous rocks that do not contain layers, and so assess when the impact of layers exerts a significant control on failure behavior, we repeat this analysis on homogeneous block models with no layers.

At each applied σ_2, we find the peak failure stress, σ_F. Rearranging the Coulomb shear failure criterion in terms of the principal stresses and uniaxial compressive strength, S_0, provides a relationship for the internal friction angle, φ (e.g., Jaeger et al., 2007):

$$\sigma_F = S_0 + \sigma_2 \tan^2\left(\frac{\pi}{2} + \frac{\varphi}{2}\right). \qquad \text{Eq. 2}$$

We find the slope of the linear regression through σ_2 and σ_F of the models to calculate φ. We report internal friction as the friction coefficient, $\mu_0 = \tan\varphi$.

4. Results

First, we describe characteristic loading curves produced by the simulated rock (Fig. 3). We analyze the distribution of σ_F and μ_0 with respect to the applied confining stress, σ_2, and layer orientation, θ, in models with block and cube geometries. We show how strain localizes as the models deform by presenting spatial distributions of particle velocities and nucleating fractures, and the difference in the percentage of fractures that form along the preexisting weaknesses and within the host matrix.

4.1. Stress-strain relationships

Typical loading curves from the numerical simulations share several characteristics with laboratory experiments (Fig. 3). Consistent with triaxial compression experiments, we observe 1) increasing failure stress, σ_F, with increasing σ_2 (e.g., Mogi et al., 1967), 2) broadening of the loading curve with approaching macroscopic failure with increasing σ_2 (e.g., Niandou et al., 1997), 3) decreasing stress drop with increasing σ_2 (e.g., Klein et al., 2001), and 4) decreasing slope of the failure envelope with increasing σ_2 (e.g., Byerlee, 1978) (Fig. 3). The decreasing slope of the failure envelope with increasing σ_2 may arise from the initial compaction of the model preceding axial displacement loading, as the initial porosity is 24-25%. These models do not produce a clear transition from brittle to ductile behavior up to 50 MPa confining stress. This transition could occur at higher confining stresses, but as this study focuses on brittle failure, we do not assess this possibility. This transition likely depends on the ratio of the normal and shear stiffness of the bonds in DEM simulations.

Calculating the linear best-fit through the failure envelope of principal stresses (σ_F and σ_2) produces values of R^2>0.95 for all of the models, lending confidence to the μ_0 estimates that we derive from the linear regression through the full range of σ_2. This linearity, and resulting high R^2 values are consistent with the R^2 values (0.90-0.99) of linear regressions of experimental failure envelopes of shale produced in direct shear tests (Heng et al., 2015). However, because previous work (e.g., Byerlee, 1978) as well as our data indicates that the slope of the failure envelope decreases at higher σ_2, we calculate μ_0 using linear regressions through the failure envelope for the subsets σ_2=0-20 MPa, and σ_2=20-50 MPa, as well as σ_2=0-50 MPa (Figs. S.4-S.5).

The curvature of the failure envelope from 0-20 MPa, in particular, suggests that estimates of internal friction using data from this range will underestimate friction at the lower end of this range. However, the relatively high R^2 values suggest that the difference between the true and apparent internal friction will be small.

4.2. Impact of layer orientation on macroscopic geomechanical behavior

The applied confining stress, σ_2, layer orientation, θ, and overlap distance control the peak failure stress, σ_F (Fig. 4). Consistent with laboratory experimental studies (e.g., Donath, 1961; Duveau et al., 1998), σ_F is lowest when θ is 60°, and maximized at 90° and 0-15° (Fig. 4). For each applied σ_2, the range of σ_F as a function of orientation is slightly greater in the block models than the cube models (Fig. 4). This result arises because the block models have higher layer interface area than the cube models. Varying the orientation of the layers therefore has a greater impact on σ_F in the block models because they have larger ratios of the number of weak bonds to strong bonds than the cube models. The range of σ_F is larger in models with smoother layer interfaces (0.2 mm overlap) than in models with rougher layer interfaces. We expect that the influence of layer orientation on failure will be magnified when the layer interfaces are smoother compared to when they are rougher. When the layer interfaces are rougher, they function more similarly to the host matrix rather than mechanical weaknesses. Notably, the σ_F for each σ_2 of models with horizontal and vertical layers are almost identical to that of the homogeneous block models.

Due to the steeping of the failure envelopes at lower σ_2 (Fig. 3), we determine μ_0 using the full σ_2 range (0-50 MPa), as well as lower (0-20 MPa) and higher (20-50 MPa) ranges (Fig. S4-S5). As expected, μ_0 calculated from the lower σ_2 range (red in Fig. 5) is larger than the upper σ_2 range (blue in Fig. 5), while the estimates derived from the full range sit between those extremes (Fig. S4-S5, black in Fig. 5). In the block models, the distribution of σ_F produces similar values of μ_0 to cube models, with minima at θ=60°, i.e., at 30° with respect to σ_1 (Fig. 5). The range of μ_0 is larger in the model with smooth than rough layer interfaces (Fig. 5).

In general, the homogeneous models produce estimates of μ_0 that closely match estimates from models with horizontal and vertical layers (Fig. 5). At confining stresses <20 MPa, the presence of layers reduces μ_0 from that of more homogeneous rock only when θ=30°-60°. At higher confining stresses, the layers produce μ_0 that differs from the homogeneous models when θ=0°-60°.

The cube models display a smaller range of μ_0 values than in the block models (Fig. 5), consistent with trend in σ_F described above, and can similarly be attributed to the reduced interface area in the cube models relative to the block models. Some trends in the distribution of μ_0 with respect to θ are similar between the block and cube models, including the maxima at 75°, and minima at 60°. However, whereas the μ_0 minimum occurs only at 60° in the block models, and in the cube models with smooth interfaces (0.2 mm overlap); in the rougher cube models, μ_0 is minimized when θ is 0°, 30° and 60° (Fig. 5).

To investigate whether the anomalously high μ_0 for models with θ=75° arises from numerical artifacts, we calculate μ_0 for block models oriented at θ=70° and θ=80° because these angles bracket θ=75°, for both smooth (0.2 mm overlap) and rough (0.5 mm overlap) interfaces. We find that the resulting μ_0 estimates when θ=70° and θ=80° similarly bracket this value at θ=75° (Fig. S6). This distribution of μ_0 suggests that the high μ_0 at θ=75° is not an artifact of the model set up, but reflects the magnified impact of σ_2 on σ_F at lower σ_2 compare to that impact at higher σ_2 for these steeper orientations (70-90°). This heightened sensitivity of σ_F to σ_2 produces steeper slopes in the failure envelopes over the full σ_2 range, and particularly from σ_2=0-20 MPa, which produces higher μ_0 when θ=70-90° (Fig. S6). As the layer orientation steepens from 60° to 80°, σ_F at each tested confining stress gradually increases (Fig. S6). However, when the layer orientation steepens from 80° to 90°, σ_F at confining stresses <20 MPa increase by larger magnitudes than those increases from 60° to 80°. This sudden jump suggests that the results at 90° are more anomalous than those at 75°. In other words, if the σ_F under lower confining stresses (<20 MPa) at 90° more closely matched those at 80°, then the trend in internal friction would more closely match expectations: gradually increasing from 60° to 90°. The applied microparameter tensile strength may have produced this anomalous result. Lower tensile strength would promote failure along planes orientation parallel to σ_1 (at 90°), producing lower σ_F at lower confining stresses and thus higher internal friction coefficients.

Similarly, Cho et al. (2012) found overlapping values of uniaxial compressive strength when θ=75° and θ=90° in laboratory tests on layered shale. The difference in layer orientation did not appear to influence the orientation of system-spanning fractures in these experiments, with both tend to trend parallel to σ_1. In our numerical simulations, the steepening of layers by 15° toward σ_1 do not significantly increase the failure strength at higher confining stresses (>30 MPa), but do lead to larger increases in strength at lower confining stresses (<30 MPa). This difference in behavior likely arises from the ability of the cores to fail via axial splitting along fractures trending vertical to σ_1 (promoted under lower confining stresses), or along more-obliquely oriented fractures (promoted under higher confining stresses).

Comparing the magnitudes of μ_0 produced in models with each of the assessed parameters held constant reveals the relative impact of each individual parameter (Fig. 6, Fig. S7). Models with the largest interface area (blocks) and the smoothest layers (0.2 mm) produce the largest changes in μ_0 (Fig. 6A). In general, smoother interfaces promote slightly lower values of internal friction than rough interfaces, with the largest variations when layers are oriented at θ=45° and 60° (Fig. 6B, D). Internal friction values are similar for cubes (with lower interface area) and blocks (with higher interface area) except for layers oriented at θ=60° and 75°, where μ_0 for the blocks and cubes diverge the most (Fig. 6C, D). Varying the layer orientation produces the largest $\Delta\mu_0$ compared to varying the layer interface roughness or model shape (Fig. 6A, D).

Varying the shape of the model (cube or block) produces the smallest changes in μ_0 relative to the layer orientation and layer roughness (Fig. 6C, D).

The distribution of elastic modulus relative to the layer orientation produced in these numerical models are consistent with laboratory experiments on layered shale (Cho et al., 2012). In both these numerical models (Fig. S8) and experiments, the effective elastic modulus increases as the orientation of layers become increasingly parallel to σ_1.

4.3. Linking microstructural deformation to macroscopic behavior

To understand how the preexisting weaknesses influence the location and organization of microscopic failure, we show the spatial distribution of particle velocities (Fig. 7) and nucleating fractures (Fig. 8) as the simulated rock begins to fail. In these models, the bonds that break in each time step are analogous to nucleating or growing fractures in natural rock, and so we refer to them as nucleating fractures. Similarly, just as microfractures coalesce to form macroscopic faults in natural rocks, many bonds may break in clusters and thus form through-going faults. Particle velocities reveal structural reorganization within the rock at a micro- and mesoscopic scale. We focus on block models with 0.2 mm overlap because these models produce the largest variation in geomechanical behavior as the layer orientation changes. We report results from two representative confining stresses (0 MPa, 10 MPa) in models with end-member layer orientations (θ=0°, 90°), and the orientation that produces the lowest σ_F and μ_0 in the block models, θ=60°.

In models with horizontal layers (θ=0°), and no confining stress, early in the experiment, the spatial distributions of particle velocities (Fig. 7A, Animation S1) and fractures (Fig. 8A, Animation S1) indicate that the weaker layer interfaces accommodate more deformation than within the layers, and later deformation spreads to the host matrix. Initially, the upper layer concentrates deformation, and then as the lower layer begins to break, bond breakage penetrates this lower layer in a diffuse volume that is bounded by inclined planes (Fig. 8A). At higher confining stress (10 MPa), the spatial distribution of particle velocities (Fig. 7D, Animation S2) and fractures (Fig. 8D, Animation S2) reveal that deformation is more equally distributed throughout the host matrix. Deformation appears to be localized onto the weak bonds between layers only early in the experiment, whereas after 0.003 of axial strain, bonds break throughout the model apparently irrespective of the location of the weaknesses (Fig. 8D). After this axial strain, the fractures align into inclined pseudo-planar volumes. The confining stress appears to suppress the influence of the weak structure. The deformation patterns produced under no and 10 MPa confining stress resemble macroscopic failure produced by the propagation of a through-going fault.

In models with layers oriented at θ=60° under zero or no confining stress, the spatial distributions of particle velocities (Fig. 7B, Animation S3) and fractures (Fig. 8B, Animation S3) indicate that a subset of the layer interfaces preferentially accommodate slip throughout much of the experiment. The few dominantly active interfaces are separated by several intermediate passive layers, causing the rock to fail as if it had fewer and thicker layers. However, velocity gradients within the emergent layers indicate that slip along the interfaces does not accommodate all of the deformation and some damage is located within the host (Fig. 7B). Early in the simulation, fractures form along all of the preexisting layer interfaces, whereas with continued strain, slip localizes onto only a few of the available slip surfaces (Fig. 8B, Animation S3). The observed strain localization onto a portion of the available surfaces suggests that the thickness of preexisting layers (i.e., the total layer interface area) does not exert a primary control on strain localization and the resulting geomechanical behavior when θ=60°. Similarly, at higher confining stress (10 MPa), the spatial distributions of particle velocities (Fig. 7E, Animation S4) and fractures (Fig. 8E, Animation S4) indicate that early in the experiment, weak bonds between layers preferentially localize deformation, but after 0.00103 axial strain, deformation localizes onto only a few interfaces.

In models with vertical layers (θ=90°) under no confining stress, the spatial distributions of particle velocities (Fig. 7C, Animation S5) and fractures (Fig. 8C, Animation S5) reveal that the vertical layers facilitate axial splitting. This macroscopic failure behavior arises from tensile failure along the layer interfaces. In addition, similar to the models with horizontal layers, inclined planes of nucleating fractures penetrate within layers later in deformation. Differences in particle velocities across layer interfaces indicate some slip across layer interfaces, but at lower magnitudes than observed in models with layers dipping at 60° (Fig. 7B). Gradients in the velocity fields within individual layers highlight that slip and opening along the interfaces and breakage in the top portion of the block did not accommodate all of the deformation within the rock. At higher confining stress (10 MPa), the spatial distributions of particle velocities (Fig. 7F, Animation S6) and fractures (Fig. 8F, Animation S6) indicate that the vertical layers do not appear to concentrate deformation along their interfaces as the rock fails, unlike the zero confining stress case. Instead, deformation gradually localizes onto an oblique fracture oriented at approximately 30° to σ_1 that accommodates both shear and tensile failure. The impact of the vertical weak interfaces, similarly to horizontal layers (Fig. 7D, Fig. 8D, Animation S2), appears to be suppressed by confining stress, perhaps because the axial splitting mechanism (Fig. 7C, Animation S5) can no longer operate as effectively under the applied confining stress.

In homogeneous models that lack preexisting layers, the spatial distributions of particle velocities and fractures (Animations S7-S8) appear similar to those observed in models with horizontal layers, consistent with the similar failure stresses and internal friction of those sets of models. In particular, under no confining stress, the rock begins to fail through the development of a broad zone of fractures at a top corner of the model that spreads into the block along a plane inclined at around 30º to σ_1.

4.4. Preferential strain localization along layer interfaces

To quantify the degree and rate of strain localization onto preexisting weaknesses relative to the host rock, we track the number of (weak) interface bonds that break in each model time step versus (strong) host rock bonds (Fig. S9, Fig. 9). We calculate the percentage of stronger host bonds (out of the total strong bonds), B_s, and the percentage of weak interface bonds (out of the total weak bonds), B_w, that break (Fig. S9). We report the difference B_w-B_s, as parameter ΔB. This parameter reveals the extent to which localized fracture development occurs along the preexisting weaknesses as opposed to within the host rock. A large value of ΔB indicates damage is preferentially localized along the weak interfaces whereas a smaller value indicates a reduced impact of the weak interfaces. The evolution of ΔB is presented as a function of the applied strain (normalized by failure strain) for the full range of tested confining stresses and interface orientations (Fig. 9). Trends are similar in block and cube models, as well as for rougher and smoother layer interfaces (Fig. S9), so we focus on the block models with smoother layer interfaces (Fig. 9).

Preceding failure in each model, ΔB is positive because the percentage of weak bonds that break are always higher than the percentage of strong bonds (Fig. 9, Fig. S9). In each model, there is an initial increase in ΔB with applied strain, but in some cases ΔB decreases as the rock approaches failure. The layer orientation exerts a stronger influence on the evolution of ΔB than the σ_2 (Fig. 9). At each σ_2, the ΔB evolution is relatively similar for constant θ (Fig. 9A-C). At differing θ, variations in σ_2 do not produce as significant changes in the overall ΔB evolution, except at higher θ (Fig. 9D-F). At higher θ, the differences are systematic, and produced by the suppression of fractures opening in the direction of the applied confining stress. In particular, the overall slope of the ΔB curve decreases as confining stress increases when the layers are vertical. The impact of σ_2 on the ΔB evolution increases with increasing θ because the applied confining stress prevents some opening along layer interfaces in models with vertical layers, and does not prevent this opening in models with more shallowly dipping layers.

The ΔB evolution reflects the impact of the microstructural reorganization and damage observed in the spatial distribution of particle velocities (Fig. 7) and fractures (Fig. 8). At lower θ (0-15°), the ΔB increases, then flattens, and decreases as the rock approaches failure (Fig. 9A-D). This decrease indicates that an increasing percentage of strong bonds relative to the percentage of weak bonds are breaking in each time step. The spatial distribution of particle velocities and fractures in the model with horizontal layers also indicate that a decreasing number of bonds break along layer interfaces throughout the experiment (Fig. 7, Fig. 8).

When θ is 60°, and σ_F and μ_0 are minimized, ΔB and the rate of ΔB continually increase preceding macroscopic failure for each σ_2. The ΔB evolution (Fig. 9), and spatial distribution of particle velocities (Fig. 7) and nucleating fractures (Fig. 8) demonstrate that slip along the layer interfaces preferentially accommodates the majority of deformation throughout the models with θ=60°. Gradients in the particle velocity fields within individual layers and the presence of fractures nucleating away from the weak interfaces demonstrate that damage in the host rock accommodates a portion of the total strain, and the ΔB evolution quantifies the degree of strain localization onto the preexisting weaknesses.

To further assess the relative influence of layer orientation and confining stress on strain localization, we calculate the anisotropy ratio K_2 (Fig. 10). Following the approach of Lisjak et al. (2014), K_2 is the ratio of the maximum to minimum differential stress at failure of experiments with equal confining stress and differing layer orientation:

$$K_2 = \frac{(\sigma_1 - \sigma_2)_{max}}{(\sigma_1 - \sigma_2)_{min}} \qquad \text{Eq. 3}$$

High K_2 indicates larger differences between the failure stresses of the weakest and strongest models. Consistent with Lisjak et al. (2014), K_2 decreases as confining stress increases, and begins to plateau when σ_2>20 MPa. Comparing the relationship between K_2 and confining stress for models with smoother and rougher layer interfaces and block- and cube-shapes indicates that smoother layer interfaces and greater interface area produce higher anisotropic ratios. This result arises because smoother layers and more area available for slip magnify the impact of the preexisting weaknesses on strain localization and subsequent failure. In addition, our comparisons of K_2 indicate that layer interface roughness more strongly controls the evolving anisotropy of macroscopic failure strength (K_2) at differing confining stresses than the model shape, and hence interface area available for slip.

5. Discussion

5.1. Influence of planar preexisting weaknesses on failure behavior

Our results constrain the manner in which preexisting mechanical weaknesses in layered rocks influence microscopic deformation that leads to macroscopic failure. Constraining the impact of heterogeneities on internal friction is critical for the robust assessment of intact material failure, and in the definition of safety factors when estimating the strength of geomaterials. We show that lower confining stress, intermediately-dipping weaknesses with respect to σ_1, smoother layer interfaces, and higher preexisting interface area available for slip magnify the impact of microscopic weaknesses on the macroscopic geomechanical behavior

(Fig. 11). Higher confining stress, more steeply or shallowly dipping weaknesses relative to σ_1, rougher interfaces and less layer interface area available for slip reduce this impact. The relative importance of each of these parameters on internal friction within the explored parameter space, from most to least important is 1) confining stress, 2) weakness orientation relative to σ_1, 3) interface roughness, and 4) interface area (Fig. 11, Fig. 6).

Previous analyses reported trends similar to those observed here between individual parameters and failure behavior, such as preexisting weakness orientation and uniaxial compressive strength (e.g., Lisjak et al., 2014). Here and in previous studies, σ_F is minimized when θ is 60°, and maximized at 90° and 0-15° (e.g., Donath, 1961; Duveau et al., 1998; Cho et al., 2012). Similarly, experimental studies have found that the internal friction coefficient is minimized at 60° and maximized at 0° and 90° (e.g., Donath, 1961; Nova, 1980). Our numerical distribution of strength relative to anisotropy orientation agrees better with experimental results than previous numerical analyses of FEM/DEM-DFN models (Lisjak et al., 2014) and DEM models (Dinç and Scholtès, 2018) that find minima in failure strength when preexisting anisotropies are oriented 45° from σ_1.

The present numerical contribution extends our understanding of the relative impact and importance of each parameter on failure behavior as well as the interplay between these parameters. Furthermore, our study directly examines the micromechanical processes that produce the resulting macroscopic behavior, and so provides insights into microstructural sources that produce particular macroscopic geomechanical behavior.

Such insights are generally not yet available experimentally without advanced techniques such as digital volume correlation (DVC) analysis of in situ microtomograms. DVC analysis provides local strain tensors within elastically and inelastically deforming material. Recent DVC analysis on experiments with laminated shale examines microscopic strain localization preceding macroscopic failure, and links the observed local strain evolution to macroscopic failure behavior (e.g., McBeck et al., 2018). These time series of local strain tensors demonstrate that the lamination bedding plane orientation of the shale controls the evolving spatial distribution of local normal strains prior to failure. Furthermore, associated numerical investigations indicate that the localization of normal strains in turn controls the localization of shear strains. These differences in the microscopic strain evolution produce differences in the macroscopic behavior: the shale core fails at a higher differential stress when its laminations are set perpendicular to σ_1 than when its laminations are subparallel to σ_1. In contrast, the uniaxial compressive strength of the present numerical models with layers set perpendicular to σ_1 are slightly lower than the strength of models with layers parallel to σ_1. This difference may arise from the lack of truncation factor used to specify the tensile strength of the bonds. In the present models, extension of the Mohr-Coulomb criterion into the tensile regime using the bond internal friction and bond cohesion determine the bond tensile strength. The application of a truncation factor reduces the bond tensile strength from that predicted from the microparameter Mohr-Coulomb criterion into the tensile regime. The measured tensile strength of rocks is often lower than that predicted from the Coulomb criterion. Although microparameter values are not expected to equal macroscopic rock values, if a truncation threshold was employed, models with layers parallel to σ_1 may have lower failure strengths than models with layers perpendicular to σ_1.

Models with the smoothest layer interfaces and greatest interface area produce the largest ranges in σ_F and μ_0. In these models, the simulated rock is geomechanically the weakest when the weaknesses are oriented at θ=60° (σ_F=40 MPa at zero confining stress), and strongest when the layers are parallel or perpendicular to σ_1 (σ_F=120 MPa at zero confining stress). Similarly, the rock has the lowest μ_0 for layers at θ=60° (0.55), and highest μ_0 for layers oriented near parallel and perpendicular to σ_1 (0.64-0.68). Estimates of μ_0 from the homogeneous models that lack layers exceed estimates of μ_0 from the layered models except when θ=70-90°. Consequently, the impact of preexisting weaknesses on μ_0 and the resulting likelihood of failure is particularly important when θ=0-60°, and less important when layers are sub-parallel to σ_1. The difference between the μ_0 calculated for the lower (0-20 MPa) and higher (20-50 MPa) σ_2 ranges is 0.15-0.2, suggesting that decreasing σ_2 by 20 MPa can increase the effective μ_0 by up to 0.2. Varying the orientation of the weaknesses may change σ_F by 66%, and μ_0 by 20% respectively.

The spatial distributions of fractures and particle velocities reveal that at low confining stress (0 MPa), the preexisting weaknesses impact both strain localization and macroscopic failure for all of the tested orientations (Fig. 7, 8). However, at higher confining stress (10 MPa), strain preferentially localizes onto the layer interfaces only when the layers are dipping at intermediate angles (θ=60°). When the layers are more shallowly or steeply dipping (θ=0° and 90°) strain effectively ignores the weak layers (Fig. 7, 8). The exploitation of the weaker layer contacts with intermediately dipping angles throughout deformation, and throughout the range of tested confining stresses, produces the lower failure stress and lower internal friction of these simulated layered rocks. Similarly, layered rocks with preexisting weaknesses at higher and lower orientations, i.e. subparallel or subperpendicular to σ_1, have higher failure stresses and higher internal friction because the microscopic deformation does not exploit the preexisting weaknesses as much as rocks with more intermediately dipping layers. This lack of exploitation causes the strength of the bulk matrix, rather than the strength of the preexisting weaknesses, to control the macroscopic strength in these rocks.

Early in the experiment when θ=60°, slip is nearly equally distributed amongst the preexisting layer interfaces, but in subsequent stages, slip localizes onto only one or two layer interfaces. This evolution produces emergent layers that are thicker than the preexisting layers. This behavior suggests that when the layers are oriented favorably for slip (θ=45°-60°), the initial width of layers may influence the onset of failure, but following the initial stage, the layer width does not significantly impact failure behavior and the macroscopic geomechanical properties.

Post-failure scanning electron microscope images of Tournemire shale provide evidence of similar interactions between preexisting weaknesses and microfractures (Bonnelye et al., 2017a). In these experiments, fractures tend to develop parallel to bedding planes when the orientation of preexisting weakness are intermediate to σ_1. When this orientation is parallel or perpendicular to σ_1, fractures typically cross cut bedding planes. This varying degree to which fractures exploit preexisting weaknesses also arises in our numerical models. These experimental results provide important validation of the microstructural deformation observed in our numerical work. Furthermore, our numerical models and experimental work (Bonnelye et al., 2017a; Holt et al., 2015) demonstrate that both confining stress and layer orientation impact the degree to which fractures exploit weaknesses.

In this numerical work, we quantify the relative impact of confining stress and layer orientation on failure behavior using ΔB (Fig. 9) and K_2 (Fig. 10). In addition, our models highlight the evolution of the degree of exploitation of preexisting weaknesses preceding failure, and not only as post-failure snapshots retrieved from experiments (e.g., Bonnelye et al., 2017a), or inferred from elastic wave measurements (e.g., Bonnelye et al., 2017b). In particular, our results enable quantitative tracking of the rate and degree of strain localization onto preexisting weaknesses relative to the host rock, ΔB, throughout loading preceding failure (Fig. 9). This quantification demonstrates that the orientation of preexisting weaknesses more strongly controls the degree and rate of strain localization than the imposed confining stress (Fig. 9). Furthermore, the degree and rate of strain localization continually increase in models with the lowest failure strengths (layers oriented 30° from σ_1), but plateau in models with higher failure strengths (layers oriented 90° from σ_1). However, in models with higher failure strengths and layers oriented parallel to σ_1, such a plateau in ΔB only occurs under higher confining stresses (>40 MPa), and an acceleration in ΔB occurs under lower confining stress. Consequently, the varying evolutions of ΔB demonstrate how the evolving spatial distribution of microfractures and their localization onto preexisting weakness planes control macroscopic failure behavior. Tracking the anisotropic ratio K_2 demonstrates that the roughness of layer interfaces exert greater control on differing failure behavior than the total layer interface area available for slip (Fig. 10).

5.2. Micromechanical models of anisotropic rock failure

Previous experimental studies have evaluated the impact of preexisting weaknesses on geomechanical behavior using laboratory data. For example, Duveau et al. (1998) compare the predictions of nine failure criteria to data from laboratory triaxial compression experiments on Angers schist. They conclude that discontinuous weakness planes models are particularly apt to capture the failure of anisotropic material because they are based on the two dominant failure mechanisms within anisotropic rock: failure along planes of weakness and failure elsewhere within the host rock. Of the discontinuous weakness planes models, our approach to evaluating the impact of weaknesses on failure is most similar to Jaeger's single plane of weakness theory (Jaeger, 1960). This formulation uses two failure envelopes following the Mohr-Coulomb failure criterion constructed from two sets of mechanical properties that represent failure along a plane of weakness or failure within the host rock. The ranges in macroscopic geomechanical properties produced by deformation of our simulated layered rock enable construction of these envelopes with end-members identified in the simulations. Using the values from block models with smoother layer interfaces when θ=60° (σ_F=40 MPa under no confining stress, μ_0=0.55) and θ=90° (σ_F=120 MPa under no confining stress, μ_0=0.68), at 7 km depth, a rotation of σ_1 from 0° to 30° from the layer orientation (or a 30° shift in the orientation of layering from σ_1) is predicted to reduce the shear stress required for failure by 104 MPa. Typical coseismic stress drops range between 1-10 MPa (e.g., Smith and Sandwell, 2003), and stress changes of 0.1 MPa may be sufficient to trigger earthquakes (King et al., 1994), indicating that a decrease in 104 MPa is significant in the context of failure of preexisting faults in the crust. When considering the failure of intact sedimentary rock, a decrease in 104 MPa is significant because it approaches estimates of the uniaxial compressive strength of sedimentary rock. These results indicate that varying the orientation of weaknesses or σ_1 can cause intact layered rock to behave as if it hosted a preexisting fault with no cohesion. Major earthquakes can rotate principal stress axes in tectonic settings (e.g., Hardebeck & Okada, 2018), and so may trigger this shift in the effective strength of the crust.

Recent analyses of series of microtomograms captured in situ throughout triaxial compression indicate that the failure of relatively isotropic and low-porosity rock (quartz-monzonite) behaves as a dynamical critical phase transition (Renard et al., 2018). Future analyses should target whether the failure of more mechanically anisotropic rock behaves critically, and/or is adequately predicted by other failure models, such as the sliding wing-crack model (Ashby & Sammis, 1990), the Drucker-Prager failure criterion (Drucker & Prager, 1952), a modified Mohr-Coulomb criterion that considers intermediate principal stresses and nonlinearity (Singh and Singh, 2011), or a discontinuous weakness planes model, such as Jaeger's criterion (Jaeger, 1960).

6. Conclusions

Constraining the impact of mechanical weaknesses on strain localization and macroscopic shear failure is critical for predicting the failure of buildings, tunnels, intact rocks, or preexisting faults. Our numerical triaxial compression experiments on layered sedimentary rock produce loading curves that broaden with increasing σ_2, stress drops that increase with increasing σ_2, and failure envelopes that decrease in slope at higher σ_2. The distributions of σ_F and μ_0 relative to the layer orientation share characteristics observed in laboratory experiments (e.g., Donath, 1961), with minimum σ_F and μ_0 near 30°, and maxima near 0° and 90° from σ_1. A 30° rotation in layer orientation (or σ_1) produces a 66% and 20% difference in σ_F and μ_0, respectively. Within the upper seismogenic zone (7 km) in a sedimentary basin, this difference in mechanical properties may decrease the shear stress required for Coulomb shear failure by 100 MPa. The degree of strain localization from along preexisting weaknesses, rather than the host rock, continually accelerates in rocks with the lowest failure strengths, but plateaus in rocks with higher failure strengths, indicating that the rate of microscopic strain localization controls macroscopic strength. Of the parameter space explored here, including layer orientation, layer interface roughness, and total layer interface area, varying the layer orientation produces the largest change in μ_0, and varying total layer interface area produces the smallest change in μ_0.

Acknowledgements

This study received funding from the Norwegian Research Council (project HADES, grant 250661) and computational resources from UNINETT Sigma2 AS, national infrastructure for computational science in Norway (project NN4557K). We thank Dion Weatherley and Steffen Abe for fruitful discussions. We thank Editor Agard and two anonymous reviewers for constructive comments that improved the manuscript.

References

Abe, S., and Mair, K. (2005), Grain fracture in 3D numerical simulations of granular shear, Geophys. Res. Lett., 32, L05305, doi:10.1029/2004GL022123.

Abe, S., and Mair, K. (2009), Effects of gouge fragment shape on fault friction: New 3D modelling results. Geophysical Research Letters, 36(23), doi: 10.1029/2009GL040684.

Abe, S., Place, D., and Mora, P. (2003), A parallel implementation of the lattice solid model for the simulation of rock mechanics and earthquake dynamics, Pure. Appl. Geophys., 161, 2265–2277, doi: 10.1007/s00024-004-2562-x.

Belheine, N., Plassiard, J. P., Donzé, F. V., Darve, F., & Seridi, A. (2009). Numerical simulation of drained triaxial test using 3D discrete element modeling. Computers and Geotechnics, 36(1-2), 320-331.

Bonnelye, A., Schubnel, A., David, C., Henry, P., Guglielmi, Y., Gout, C., Fauchille, A. & Dick, P. (2017a). Strength anisotropy of shales deformed under uppermost crustal conditions. Journal of Geophysical Research: Solid Earth, 122(1), 110-129.

Bonnelye, A., A. Schubnel, C. David, P. Henry, Y. Guglielmi, C. Gout, A.-L. Fauchille, and P. Dick (2017b), Elastic wave velocity evolution of shales deformed under upper- most crustal conditions, *J. Geophys. Res. Solid Earth*, *122*, 130–141, doi:10.1002/2016JB013540.

Byerlee, J. (1978). Friction of rocks. Pure and applied Geophysics, 116(4), 615-626.

Cundall, P. A., and O. Strack (1979), A discrete numerical model for granular assemblies, Geotechnique, 29, 47–65.

Cho, J. W., Kim, H., Jeon, S., & Min, K. B. (2012). Deformation and strength anisotropy of Asan gneiss, Boryeong shale, and Yeoncheon schist. International Journal of Rock Mechanics and Mining Sciences, 50, 158-169, doi: 10.1016/j.ijrmms.2011.12.004.

Courant, R., Friedrichs, K., & Lewy, H. (1928). On the partial difference equations of mathematical physics. Mathematische Annalen, 100.

Dinç, Ö., & Scholtès, L. (2018). Discrete Analysis of Damage and Shear Banding in Argillaceous Rocks. Rock Mechanics and Rock Engineering, 51(5), 1521-1538.

Donath, F. A. (1964). Strength variation and deformational behavior in anisotropic rock. State of Stress in the Earth's Crust, 281-298, edited by W. R. Judd, pp. 281– 297, Elsevier Sci., New York.

Donath, F. A. (1961). Experimental study of shear failure in anisotropic rocks. Geological Society of America Bulletin, 72(6), 985-989.

Drucker, D. C., & Prager, W. (1952). Soil mechanics and plastic analysis or limit design. Quarterly of Applied Mathematics, 10(2), 157-165.

Duveau, G., Shao., J., & Henry, J. (1998). Assessment of some failure criteria for strongly anisotropic geomaterials. Mechanics of Cohesive-frictional Materials, 3(1), 1-26.

Fjær, E., & Nes, O. M. (2014). The impact of heterogeneity on the anisotropic strength of an outcrop shale. Rock mechanics and rock engineering, 47(5), 1603-1611, doi: 10.1007/s00603-014-0598-5.

Gale, J. F., Laubach, S. E., Olson, J. E., Eichhubl, P., & Fall, A. (2014). Natural fractures in shale: A review and new observations. AAPG bulletin, 98(11), 2165-2216, doi: 10.1306/08121413151.

Hardebeck, J. L., & Okada, T. (2018). Temporal Stress Changes Caused by Earthquakes: A Review. Journal of Geophysical Research: Solid Earth, 123, 1350-1365. doi:10.1002/2017JB014617.

Hazzard, J. F., and Mair, K. (2003). The importance of the third dimension in granular shear, Geophys. Res. Lett., 30(13), 1708, doi:10.1029/2003GL017534.

Hentz, S., Daudeville, L., & Donzé, F. V. (2004). Identification and validation of a discrete element model for concrete. Journal of engineering mechanics, 130(6), 709-719.

Heng, S., Guo, Y., Yang, C., Daemen, J. J., & Li, Z. (2015). Experimental and theoretical study of the anisotropic properties of shale. International Journal of Rock Mechanics and Mining Sciences, 74, 58-68.

Holt, R. M., Fjær, E., Stenebråten, J. F., & Nes, O. M. (2015). Brittleness of shales: relevance to borehole collapse and hydraulic fracturing. Journal of Petroleum Science and Engineering, 131, 200-209.

Jaeger, J.C. (1960). Shear failure of anisotropic rocks. Geological Magazine, 97(1), 65-72.

Jaeger J., Cook, N., & Zimmerman, R. (2007). Fundamentals of rock mechanics. 4th ed. Oxford: Blackwell.

King, G. C. P., Stein, R. and Lin, J. (1994). Static stress changes and the triggering of earthquakes, Bull. Seismol. Soc. Am., 84, 935– 953.

Klein, E., Baud, P., Reuschlé, T., & Wong, T. F. (2001). Mechanical behaviour and failure mode of Bentheim sandstone under triaxial compression. Physics and Chemistry of the Earth, Part A: Solid Earth and Geodesy, 26(1-2), 21-25.

Lisjak, A., Tatone, B. S., Grasselli, G., & Vietor, T. (2014). Numerical modelling of the anisotropic mechanical behaviour of Opalinus clay at the laboratory-scale using FEM/DEM. Rock mechanics and rock engineering, 47(1), 187-206.

Mair, K., and Abe, S. (2008). 3D numerical simulations of fault gouge evolution during shear: Grain size reduction and strain localization, Earth Planet. Sci. Lett., 274, 72– 81, doi:10.1016/j.epsl.2008.07.010.

Mair, K., & Hazzard, J. F. (2007). Nature of stress accommodation in sheared granular material: Insights from 3D numerical modeling. Earth and Planetary Science Letters, 259(3-4), 469-485.

Mair, K., Main, I., & Elphick, S. (2000). Sequential growth of deformation bands in the laboratory. Journal of Structural Geology, 22(1), 25-42.

McBeck, J., Kobchenko, M., Hall, S., Tudisco, E., Cordonnier, B., Meakin, P., & Renard, F. Investigating the onset of strain localization within anisotropic shale using digital volume correlation of time-resolved X-ray microtomography images. Journal of Geophysical Research: Solid Earth. https://doi.org/10.1029/2018JB015676.

Mogi, K. (1967). Effect of the intermediate principal stress on rock failure. Journal of Geophysical Research, 72(20), 5117-5131.

Niandou, H., Shao, J. F., Henry, J. P., & Fourmaintraux, D. (1997). Laboratory investigation of the mechanical behaviour of Tournemire shale. International Journal of Rock Mechanics and Mining Sciences, 34(1), 3-16.

Nova, R. (1980). The failure of transversely isotropic rocks in triaxial compression. In International Journal of Rock Mechanics and Mining Sciences & Geomechanics Abstracts (Vol. 17, No. 6, pp. 325-332). Pergamon.

Nova, R., and Zaninetti, A. (1990). An investigation into the tensile behavior of a schistose rock, Int. J. Rock Mech. Min. Sci., 27, 231–242.

Pollard, D., & Aydin, A. (1988). Progress in understanding jointing over the past century, Geological Society of America Bulletin, 100, 1181-1204.

Rawling, G. C., Baud, P. and Wong, T. (2002). Dilatancy, brittle strength, and anisotropy of foliated rocks: Experimental deformation and micromechanical modeling, J. Geophys. Res., 107(B10), 2234, doi:10.1029/2001JB000472.

Renard, F., Mair, K., & Gundersen, O. (2012). Surface roughness evolution on experimentally simulated faults. Journal of Structural Geology, 45, 101-112, doi:10.1016/j.jsg.2012.03.009.

Renard, F., Weiss, J., Mathiesen, J., Ben Zion, Y., Kandula, N., & Cordonnier, B. (2018). Critical evolution of damage toward system-size failure in crystalline rock. Journal of Geophysical Research: Solid Earth, 123, https://doi.org/10.1002/2017JB014964.

Shea, W. T., and Kronenberg, A.K., (1993). Strength and anisotropy of foliated rocks with varied mica contents, J. Struct. Geol., 15, 1097–1121.

Scholtès, L. U. C., & Donzé, F. V. (2012). Modelling progressive failure in fractured rock masses using a 3D discrete element method. International Journal of Rock Mechanics and Mining Sciences, 52, 18-30.

Scholtès, L., & Donzé, F. V. (2013). A DEM model for soft and hard rocks: role of grain interlocking on strength. Journal of the Mechanics and Physics of Solids, 61(2), 352-369.

Schöpfer, M. P., Abe, S., Childs, C., & Walsh, J. J. (2009). The impact of porosity and crack density on the elasticity, strength and friction of cohesive granular materials: insights from DEM modelling. International Journal of Rock Mechanics and Mining Sciences, 46(2), 250-261.

Smith, B., & Sandwell, D. (2003). Coulomb stress accumulation along the San Andreas Fault system. J. of Geophysical Research: Solid Earth, 108(B6), doi:10.1029/2002JB002136.

Stanchits, S., Vinciguerra, S. & Dresen, G. (2006). Ultrasonic velocities, acoustic emission characteristics and crack damage of basalt and granite, Pure Appl. Geophys., 163, 975-994.

Tavallali, A., and Vervoort, A., (2010). Effect of layer orientation on the failure of layered sandstone under Brazilian test conditions. International Journal of Rock Mechanics & Mining Sciences, 47, 313-322.

Tse, R., & Cruden, D. M. (1979). Estimating joint roughness coefficients. In International journal of rock mechanics and mining sciences & geomechanics abstracts (Vol. 16, No. 5, pp. 303-307). Pergamon.

Weatherley, D. K., Boros, V. E., Hancock, W. R., & Abe, S. (2010). Scaling benchmark of ESyS-Particle for elastic wave propagation simulations. In e-Science (e-Science), 2010 IEEE Sixth International Conference on (pp. 277-283). IEEE.

Figure 1

Models of blocks with all tested layer orientations, θ, defined as the orientation of the normal to the layer interface plane with respect to σ_1. Length and width of blocks are 20 mm, and height is 40 mm. Layers are 5 mm thick. σ_1 is vertical, σ_2 and σ_3 are horizontal, and $\sigma_2=\sigma_3$. Geometries shown here have 0.5 mm overlap between layers. Colors highlight the distinct layers and the orientation of preexisting weaknesses that separate each layer. All layers have identical bulk strength. See Fig. S1 for details of the particle packing technique.

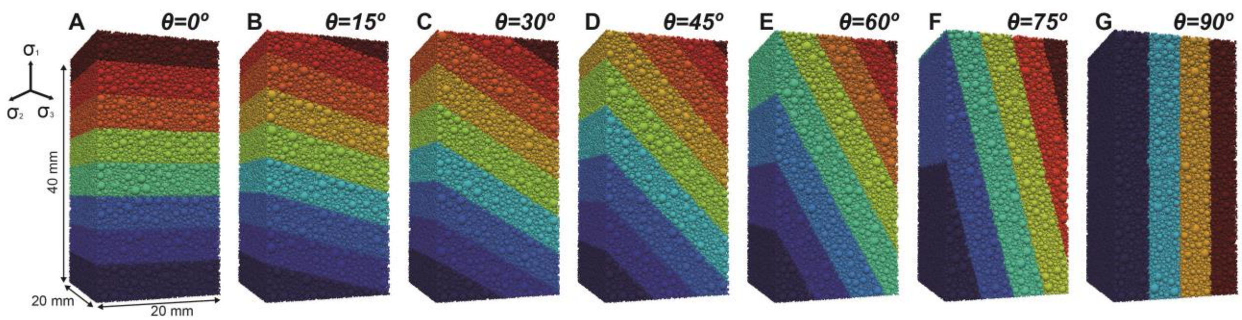

Figure 2

Surface topography of layer interfaces with 0.2 mm overlap (A-B), and 0.5 mm overlap (C-D) for block model with layers orientated 45°. A, C) Topography of bottom surface of layer interface. B, D) Topography of top surface of layer interface. We measure the topography as the distance between particle surfaces and a basal plane at the same orientation of the layers. The bottom surfaces are smoother, with lower root-mean-squared roughness, χ_{RMS}, because we pack layers starting from the bottom layer and work upward. With smaller overlap (0.2 mm), the layer interfaces are smoother (χ_{RMS}=0.028 for the bottom surface) than with larger overlap (0.5 mm, χ_{RMS}=0.055 for the bottom surface). Each topography coloring scheme ranges from the median of the topography field ± 0.1 mm.

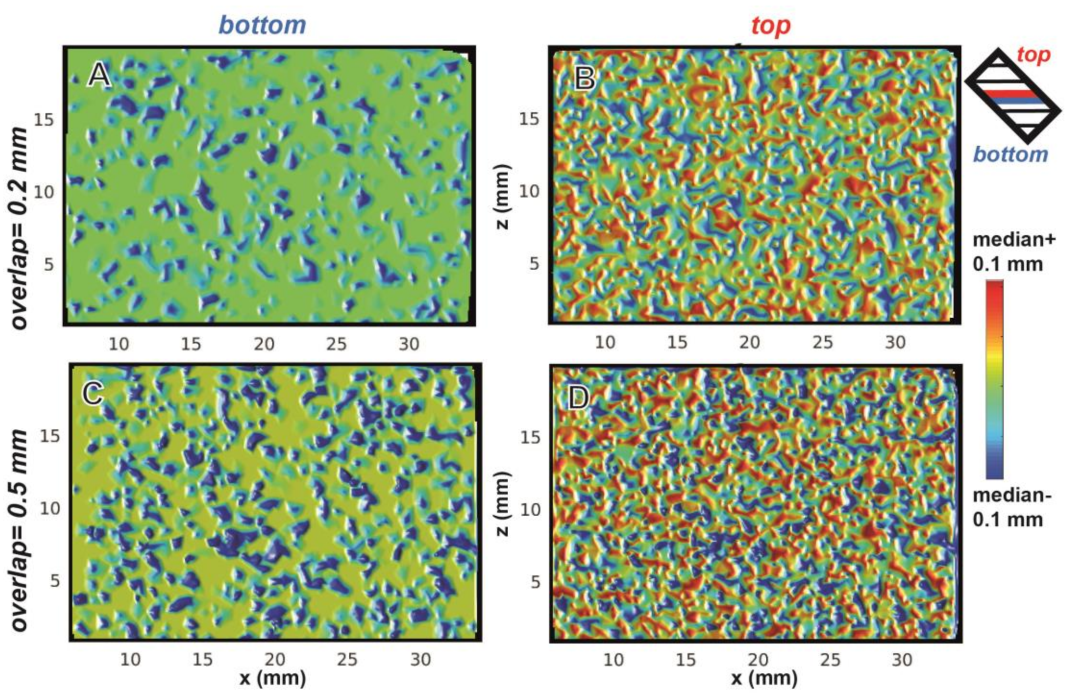

Figure 3

Mechanical loading behavior for numerical triaxial compression simulations. Results from block model with layers oriented at θ=90° and with rougher layer interfaces (0.5 mm overlap) are shown. A) Axial contraction versus differential stress for confining stresses 0-50 MPa. Squares show failure stress, σ_F, i.e., the peak stress preceding failure and the first stress drop, and vertical lines show axial contraction at failure. B) Resulting relationship between applied confining stress, σ_2, and σ_F including the linear regression from which we estimate μ_0. The slope of the failure envelope of σ_2 and σ_F decreases with increasing σ_2, and so is slightly non-linear.

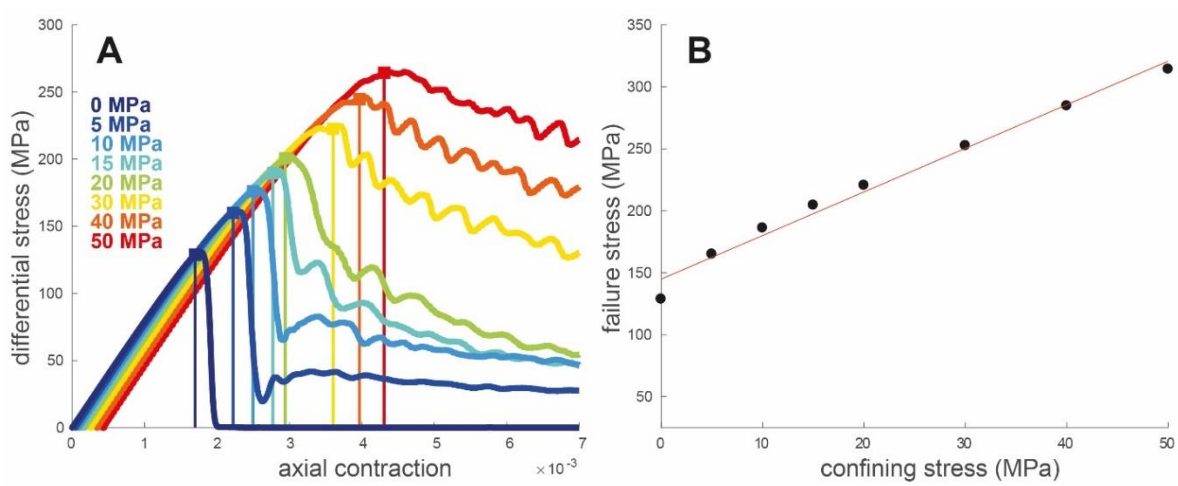

Figure 4

Distribution of σ_F as a function of σ_2 and θ for (A, B) smoother layer interfaces (0.2 mm overlap) and (C, D) rougher layer interfaces (0.5 mm overlap), and (A, C) cube and (B, D) block geometries. Results from lower (0-20 MPa), median (20 MPa), and higher (20-50 MPa) σ_2 ranges are shown in red, black, and blue, respectively. Triangles show results from homogeneous block model that does not contain layers.

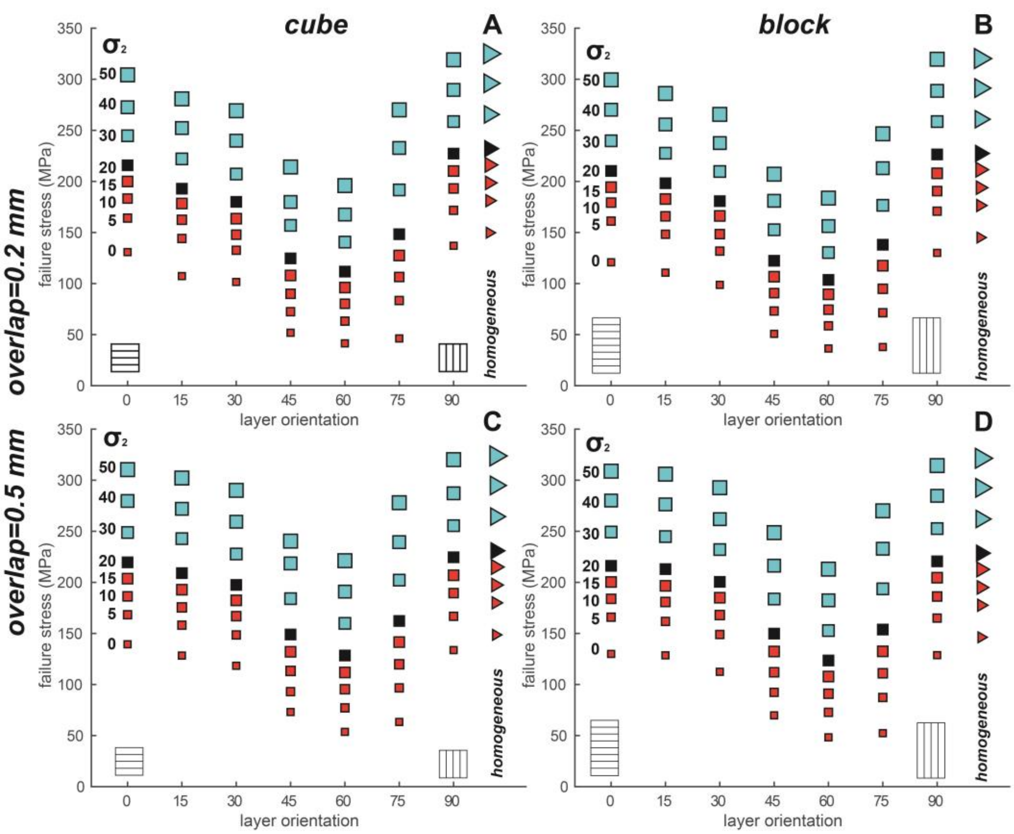

Figure 5

Distribution of μ_0 as a function of σ_2 and θ, for (A, B) smoother layer interfaces (0.2 mm overlap) and (C, D) rougher layer interfaces (0.5 mm overlap), and (A, C) cube and (B, D) block geometries. μ_0 calculated from higher (20-50 MPa), lower (0-20 MPa), and full (0-50 MPa) σ_2 range shown in blue, red and black, respectively. Horizontal lines show results from homogeneous block model that does not contain layers.

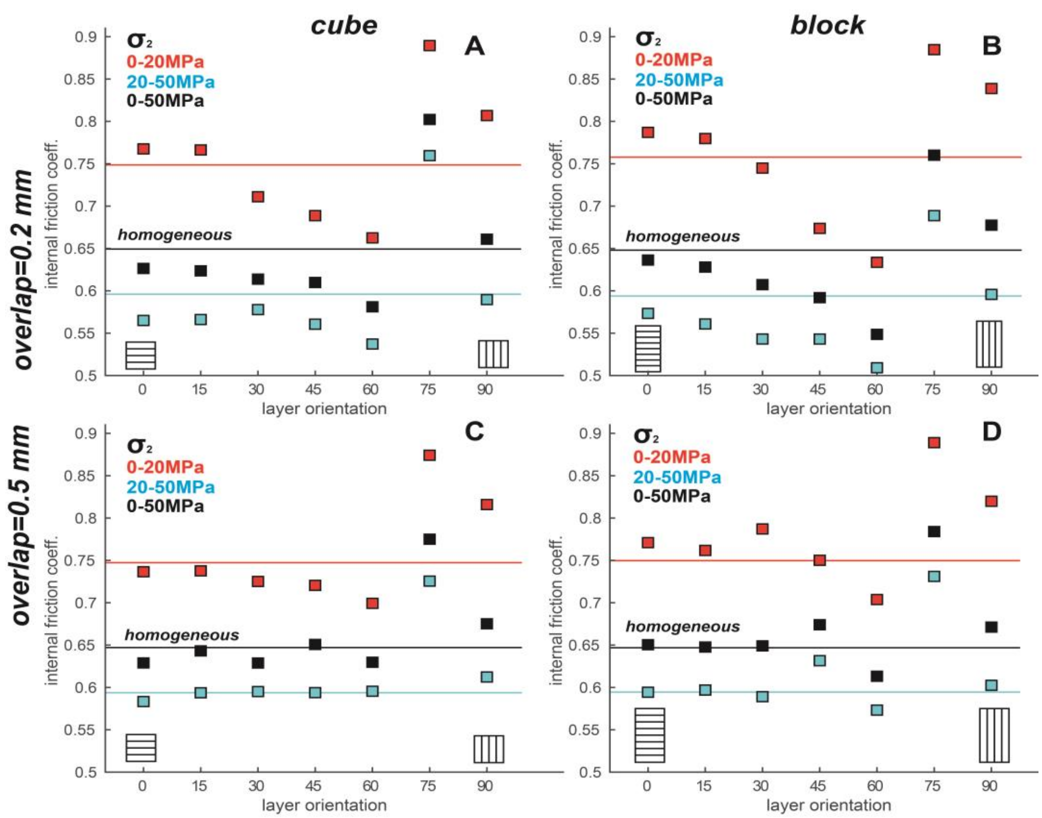

Figure 6

Relative impact of parameters on failure: (A) interface orientation, (B) interface roughness, (C) interface area (i.e., model shape). D) Difference in maximum and minimum μ_0 of each set of models comparing area (C) and roughness (B), and the difference in μ_0 when θ=90° and the minimum μ_0 (A). A) Color of symbol indicates layer orientation. B) Results from block models with 0.5 mm overlap (black) and 0.2 mm overlap (white). C) Results from models with 0.2 mm overlap with cube shapes (squares) and block shapes (triangle). D) Impact of parameters on the difference in μ_0. Varying θ produces the largest $\Delta\mu_0$, even discounting when θ=75°. Varying the layer interface area (model shape) produces the smallest $\Delta\mu_0$. Fig. S8 compares results from all of the models.

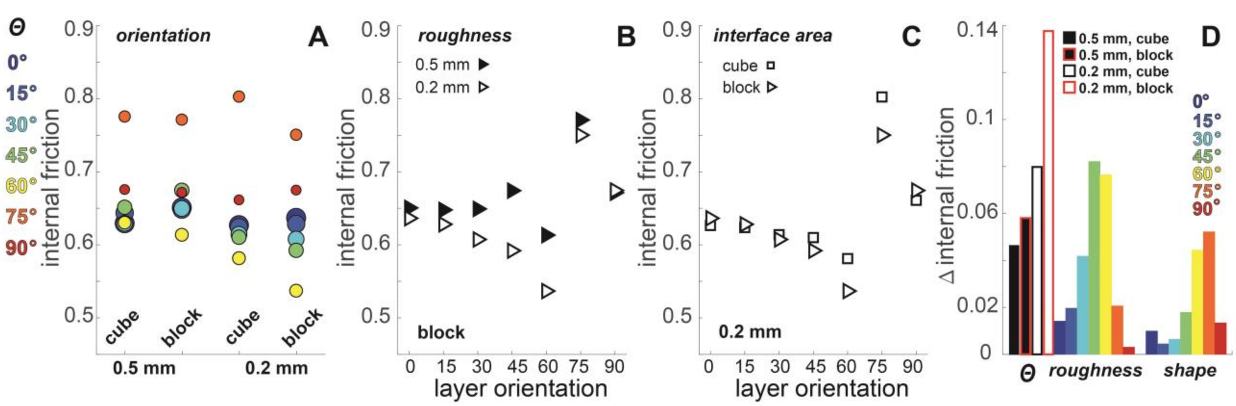

Figure 7

Spatial distributions of particle velocities highlight the influence of θ and σ_2 on strain distribution along interfaces and within host. Failure of simulated layered rock with σ_2=0 MPa, and (A) θ=0°, (B) θ=60°, and (C) θ=90°, and with σ_2=10 MPa and (E) θ=0°, (F) θ=60°, and (G) θ=90°. Black numbers are the accumulated axial strain, which increase toward the right. Colors show the total magnitude of the velocity of particles. Block models with 0.2 mm overlap are shown.

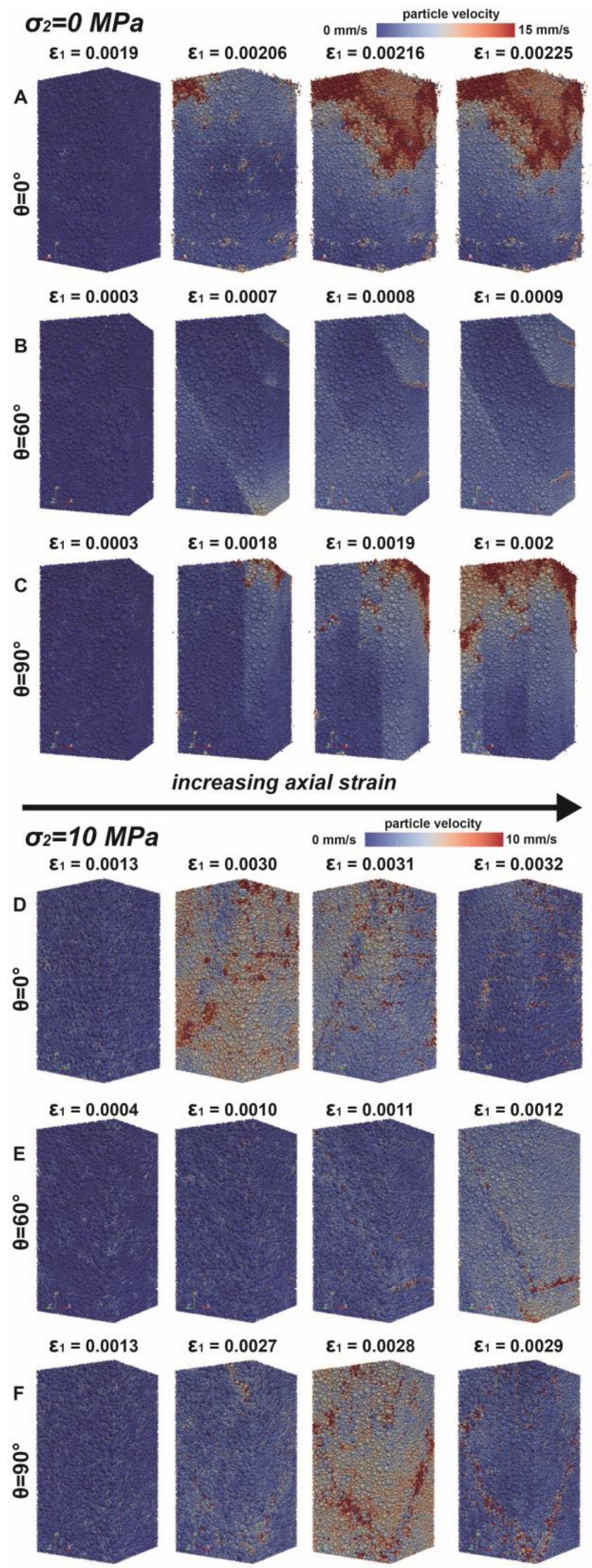

Figure 8

Spatial distributions of nucleating fractures highlight the influence of θ and σ_2. Failure of simulated layered rock with σ_2=0 MPa, and (A) θ=0°, (B) θ=60°, and (C) θ=90°, and with σ_2=10 MPa and (D) θ=0°, (E) θ=60°, and (F) θ=90°. Black numbers are the accumulated axial strain. Black lines show location of bonds that break at each time interval, i.e., nucleating fractures. Block models with 0.2 mm overlap are shown.

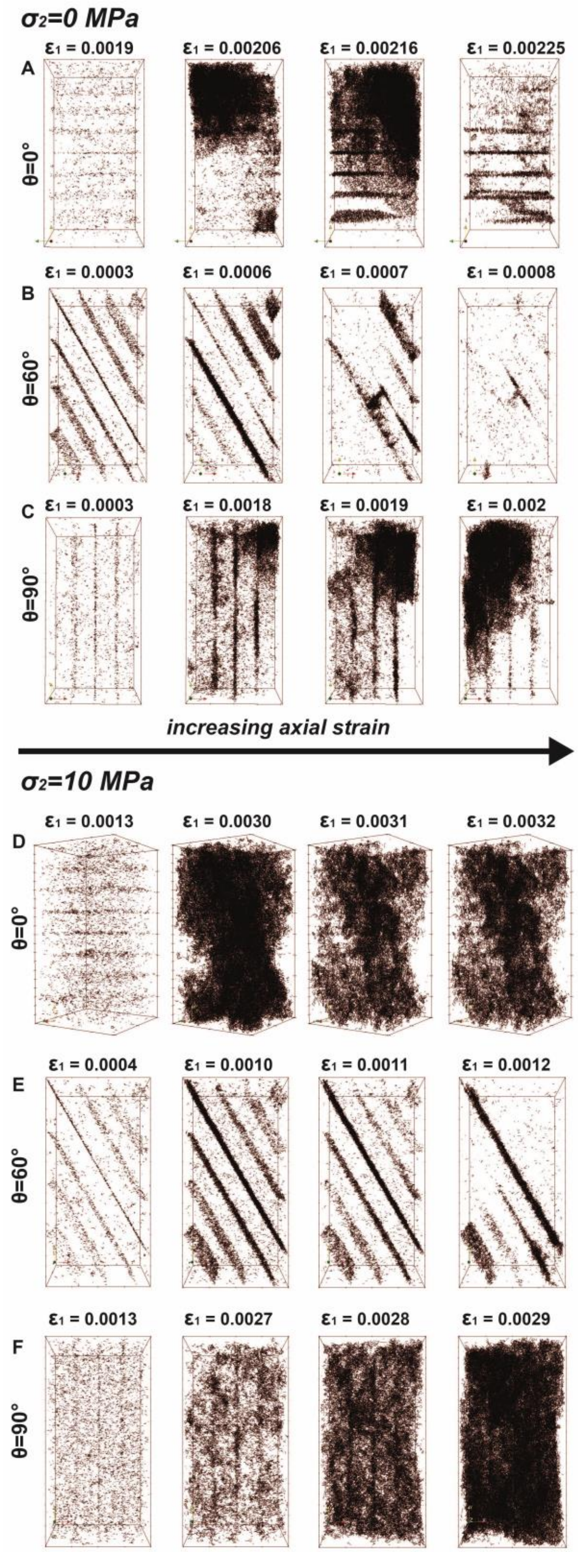

Figure 9

Evolution of failure, characterized as ΔB, indicates the relative impact of fracturing along weak interfaces compared to within the host rock. Failure localization, ΔB, is shown as the difference between the percentage of weak bonds broken out of all the weak bonds, and the percentage of the strong bonds broken out of all the strong bonds for a representative range of σ_2: (A) σ_2=0 MPa, (B) σ_2=20 MPa, and (C) σ_2=50 MPa with all tested layer orientations, θ, and for a representative range of θ: (D) θ=0°, (E) θ=60°, (F) θ=90°, and all tested σ_2. A-C) Color of lines correspond to θ. D-F) Color of lines correspond to σ_2. Data are presented for smoother layer interfaces (0.2 mm overlap) of block models.

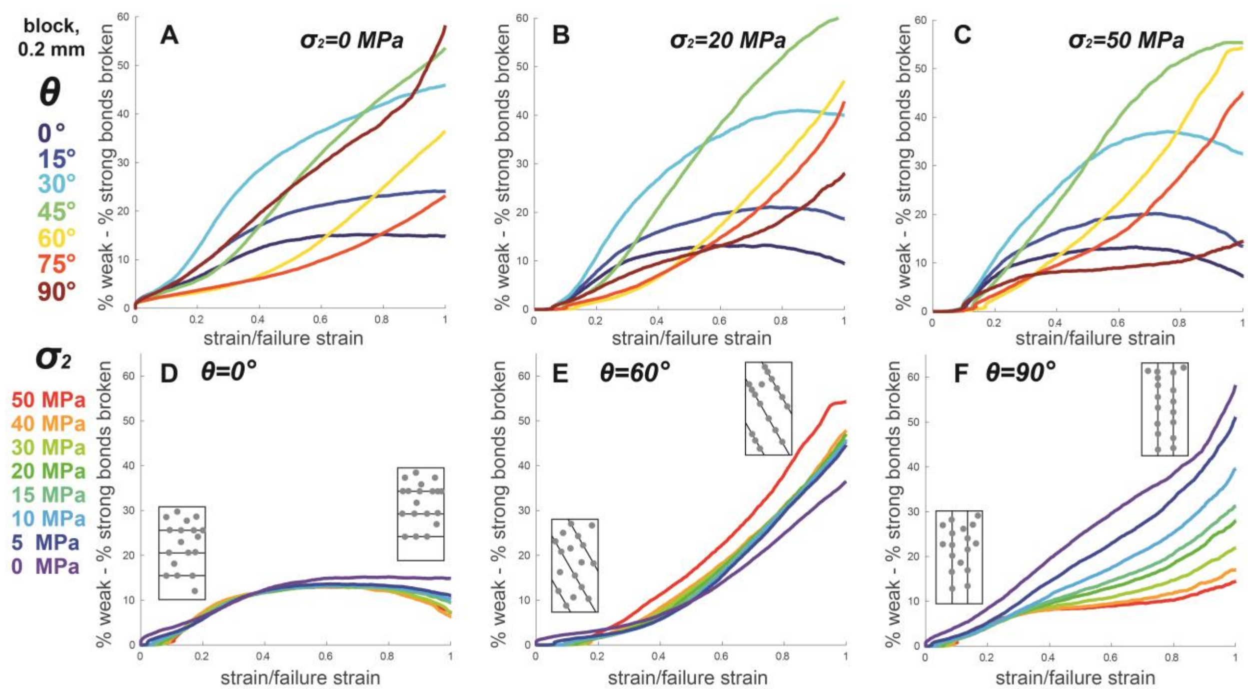

Figure 10

Evolution of anisotropic ratio, K_2, for models with varying layer interface roughness and area available for slip. Following Lisjak et al. (2014), K_2 is the ratio between the maximum and minimum differential stress at failure for experiments with different layer orientations, and constant confining stress (Eq. 3). Models with smoother layers (0.2 mm overlap, red and yellow squares) behave more anisotropically than models with rougher layers (0.5 mm overlap, light and dark blue squares). Models with block shapes (red and dark blue squares) behave more anisotropically than models with cube shapes (yellow and light blue squares), as expected from the larger difference in area available for slip in block models. Increasing confining stress suppresses anisotropic behavior.

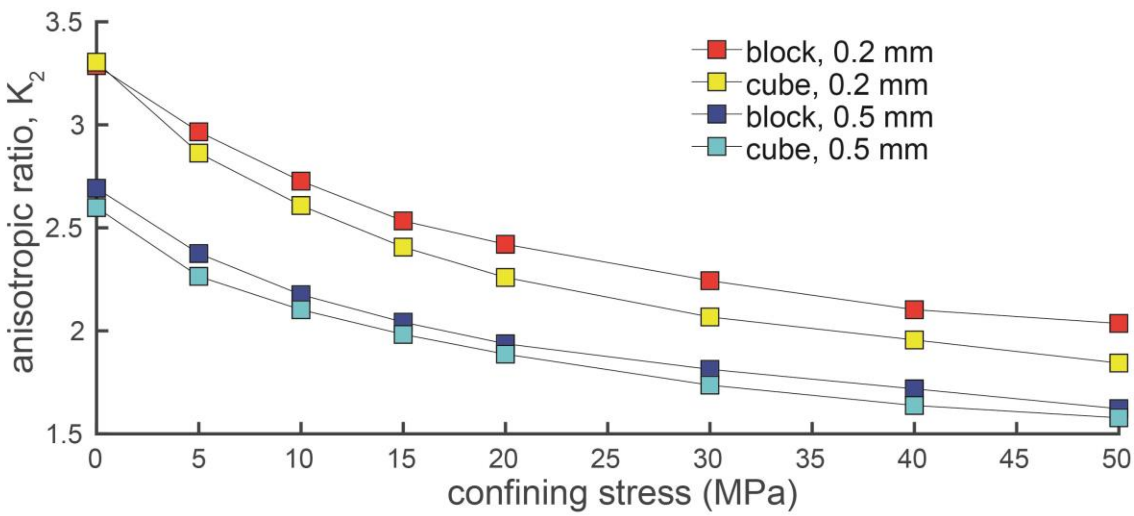

Figure 11

Sketch summarizing the relative importance of preexisting weakness property on the macroscopic μ_0. Preexisting weaknesses produce greater changes in μ_0 at lower confining stress, at intermediate layer orientations relative to σ_1, with smoother layer interfaces, and with greater total layer interface area. Varying the orientation produces the largest changes in μ_0, and varying the interface area produces the smallest changes in μ_0 over the range of parameter space explored here.